ELSEVIER

Engineering Analysis with Boundary Elements 30 (2006) 205–217

ENGINEERING ANALYSIS *with* BOUNDARY ELEMENTS

www.elsevier.com/locate/enganabound

# Null-field Integral Equations for Stress Field around Circular Holes under Antiplane Shear

Jeng-Tzong Chen *, Wen-Cheng Shen, An-Chien Wu

*Department of Harbor and River Engineering National Taiwan Ocean University Keelung 20224, Taiwan*

Received 1 June 2005; accepted 12 August 2005
Available online 6 January 2006

**Abstract**

In this paper, we derive the null-field integral equation for a medium containing circular cavities with arbitrary radii and positions under uniformly remote shear. To fully capture the circular geometries, separate expressions of fundamental solutions in the polar coordinate and Fourier series for boundary densities are adopted. By moving the null-field point to the boundary, singular integrals are transformed to series sums after introducing the concept of degenerate kernels. The solution is formulated in a manner of a semi-analytical form since error purely attributes to the truncation of Fourier series. The two-hole problems are revisited to demonstrate the validity of our method. The bounded-domain approaches using either displacement or stress approaches are also employed. The proposed formulation has been generalized to multiple cavities in a straightforward way without any difficulty.


*Keywords:* antiplane deformation; null-field integral equation; degenerate kernel; Fourier series; circular hole; Laplace problem

## 1. Introduction

Researchers and engineers have paid much attention on the development of boundary integral equations (BIEs) and boundary element method (BEM) since Rizzo [15] proposed a numerical treatment for elastostatics. Most of the efforts have been focused on the singular boundary integral equation for problems with ordinary boundaries. In some situations, the singular boundary integral equation is not sufficient, *e.g.* degenerate boundary, fictitious frequency and spurious eigenvalue. Therefore, the hypersingular equation is required. The role of hypersingularity in computational mechanics has been examined in the review article of Chen and Hong [5]. In the past, several regularizations for singularity and hypersingularity were offered to handle it in direct and indirect ways. Hong and Chen [4] have developed the theory of dual boundary integral equation method (BIEM) and dual BEM with hypersingular kernels. The analytical formula reveals the jump behavior of double layer potentials. How to determine accurately the free terms has received more attentions in the past decade. Two conventional approaches were employed to regularize the singular and hypersingular integrals. First, Guiggiani [9] has derived the free terms for Laplace and Navier equations using bump approach in Fig. 1 (a). Second, Gray and Manne [8] have employed a limiting process to ensure a unique solution from an interior point to boundary in Fig. 1 (b). In the present approach, we employed the degenerate kernel for the two-point fundamental solution in the problems with circular boundaries as shown in Fig. 1 (c).

More recently, Honein *et al.* have solved problems of two arbitrary circular holes or rigid inclusions [10–12] of different shear moduli under uniformly remote shear. They have introduced the Möbius transformations involving the complex potential to analytically investigate the stress field around the hole. The extension to more than two holes may have difficulty in the Honein's formulation. To search a systematic method for multiple circular holes is not trivial. It is found that the tangential shear stress $\sigma_{\theta z}$ at the closest points of the two circular holes tends to infinity as the two cavities approach each other. Mogilevskaya and Crouch [14] have solved the problem of an infinite plane containing arbitrary number of circular inclusions based on the complex singular integral equation. In their analysis procedure, the unknown tractions are approximated by using complex Fourier series. The advantage of their method is that one can tackle a lot of inclusions even inclusions touching one another. However, for calculating an integral over a circular boundary, they did not

* Corresponding author. Tel: +886-2-24622192 ext. 6177; fax: +886-2-24632375.
*E-mail address:* jtchen@mail.ntou.edu.tw (J.-T. Chen).

0955-7997/$ - see front matter © 2005 Elsevier Ltd. All rights reserved.
doi:10.1016/j.enganabound.2005.08.013

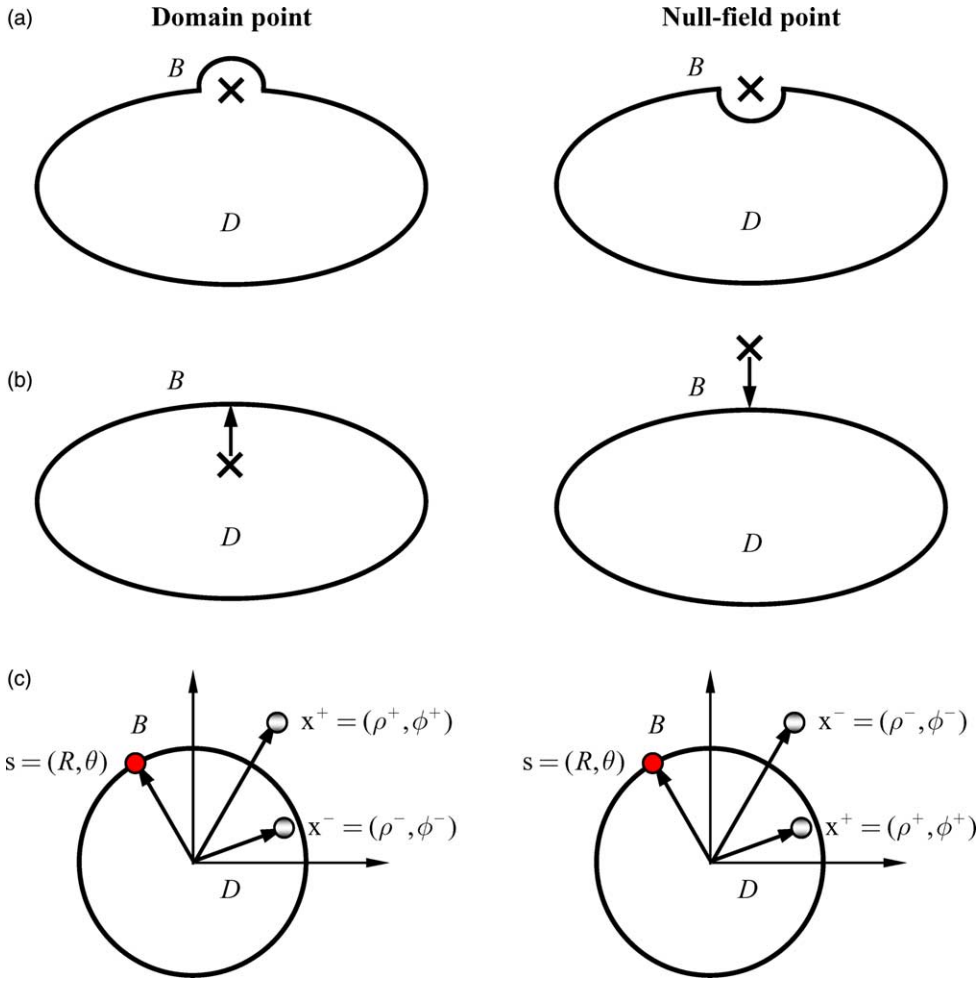


Fig. 1. (a) Bump contour, (b) Limiting process, (c) Present method.

express the fundamental solution using local polar coordinates. By collocating the null-field point on the boundary, the singular integral can be easily determined using series sums in our formulation due to the introduction of degenerate kernels.

Since the analytical solution for more than two cavities may encounter difficulty, several numerical approaches have been employed, *e.g.* complex variable boundary element method (CVBEM) by Chou [7] and Ang and Kang [1]. The CVBEM was primarily introduced by Hromadka and Lai [13] for solving the Laplace problems in an infinite domain. In 1997, Chou extended the work of Hromadka to the multiply connected domain in an infinite plane. The antiplane problem with holes can be formulated in terms of derivatives of displacement. Thus, the stresses around the hole had been obtained directly without resource to numerical differentiation. Recently, Ang and Kang [1] developed a general formulation for solving the second-order elliptic partial differential equation for a multiply-connected region in a different version of CVBEM. The Cauchy integral formulae are offered to solve the exterior boundary value problem [2]. By introducing the CVBEM, Chou [7] and Ang and Kang [1] have revisited the problems with two circular holes whose centers lie on the $x$ axis investigated by Honein *et al.*. Bird and Steele [3] used a Fourier series procedure to solve the antiplane elasticity problems in Honein's paper [11]. To approximate the Honein's infinite problem, an equivalent bounded-domain approach with stress applied on the outer boundary was utilized. A shear stress $\sigma_{rz}$ on the outer boundary is used in place of a stress $\sigma_{32}$ at infinity to approach the Honein's results as the radius becomes large.

Since the cavity or inclusion is circular, we may wonder why not using the degenerate kernels in the polar coordinate and Fourier series to best fit the geometry. In this paper, a semi-analytical approach is successfully developed to carry out the solution of the problem under antiplane shear. The mathematical formulation is derived by using degenerate kernels for the fundamental solution and Fourier series expansions for the boundary densities in the null-field integral equation. Then, it is reduced to a linear algebraic system after collocating points on each circular boundary and substituting the boundary conditions. The unknown coefficients in the algebraic system can be determined. Furthermore, arbitrary number of circular holes can be treated by using the present method without any difficulty. A general purpose program for arbitrary number of holes with various radii and different positions was developed.

## 2. Formulation of the problem

The displacement field of the antiplane deformation is defined as:

$$u = v = 0, \quad w = w(x, y), \tag{1}$$

where $w$ is the only nonvanishing component of displacement with respect to the Cartesian coordinate which is a function of $x$ and $y$. For a linear elastic body, the stress components are

$$\sigma_{13} = \sigma_{31} = \mu \frac{\partial w}{\partial x}, \tag{2}$$

$$\sigma_{23} = \sigma_{32} = \mu \frac{\partial w}{\partial y}, \tag{3}$$

where $\mu$ is the shear modulus. The equilibrium equation can be simplified to

$$\frac{\partial \sigma_{31}}{\partial x} + \frac{\partial \sigma_{32}}{\partial y} = 0. \tag{4}$$

Thus, we have

$$\frac{\partial^2 w}{\partial x^2} + \frac{\partial^2 w}{\partial y^2} = \nabla^2 w = 0. \tag{5}$$

What is taken into consideration is an infinite medium subject to $N$ traction-free circular holes bounded by the $B_k$ contour and $k = 1, 2, \ldots, N$ as shown in Fig. 2. The medium is under uniformly remote shear stress $\sigma_{31}^{\infty} = 0$, $\sigma_{32}^{\infty} = \tau$ at infinity or equivalently under the displacement

$$w^{\infty} = \frac{\tau y}{\mu}. \tag{6}$$

The total stress field in the medium is made to be decomposed into

$$\sigma_{31} = \sigma_{31}^{s} + \sigma_{31}^{\infty}, \tag{7}$$

$$\sigma_{32} = \sigma_{32}^{s} + \sigma_{32}^{\infty}, \tag{8}$$

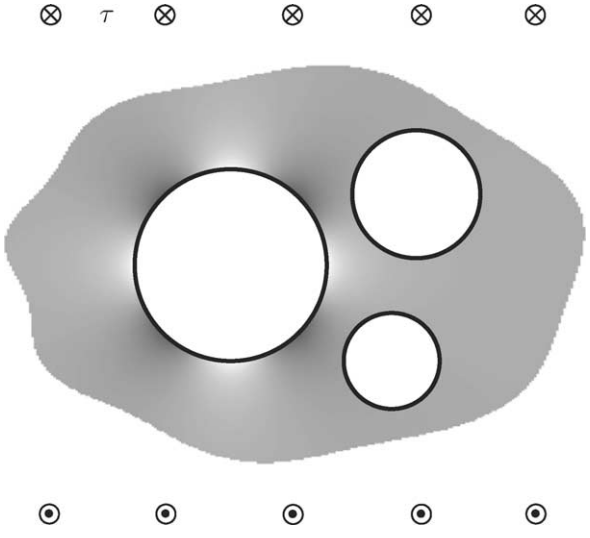


Fig. 2. Infinite antiplane problem with arbitrary traction-free circular holes.

and the total displacement can be given as

$$w = w^{s} + w^{\infty}, \tag{9}$$

where the superscript "$s$" denotes the part needed to be solved after decomposition. Therefore, the antiplane problem is reduced to find the displacement $w^s$ which satisfies the Laplace equation and the Neumann boundary conditions that will be elaborated on later. The problem can be converted into the solution of the Laplace problem for $w^s$:

$$\nabla^2 w^{s}(x) = 0, \quad x \in D, \tag{10}$$

and the traction-free condition results in the following Neumann boundary condition

$$\frac{\partial w^{s}(x)}{\partial \mathbf{n}} = -\frac{\tau}{\mu} n_y, \quad x \in B_k, \tag{11}$$

where the unit outward normal vector on the hole is $\mathbf{n} = (n_x, n_y)$. It is convenient to display the stress components in the polar coordinate since the fundamental solutions are separated in the system. The shear stress components, $\sigma_{rz}$ and $\sigma_{\theta z}$, can be superimposed by using $\sigma_{31}$ and $\sigma_{32}$

$$\sigma_{rz} = \mu \frac{\partial w}{\partial \mathbf{n}}, \tag{12}$$

$$\sigma_{\theta z} = \mu \frac{\partial w}{\partial \mathbf{t}}, \tag{13}$$

where $\mathbf{n}$ and $\mathbf{t}$ are the normal and tangent directions. Before determining $\sigma_{rz}$ and $\sigma_{\theta z}$ on the interior point, we should calculate $\sigma_{31}^{s}$ and $\sigma_{32}^{s}$ by implementing the hypersingular equation in the real computation. For shear stress $\sigma_{\theta z}$ on the boundary, the same procedure of vector decomposition is required.

In order to avoid decomposing the $w$ field into two parts, Bird and Steele [3] have used a bounded-domain approach with the equivalent stress $\sigma_{rz} = \sin\theta$ on the artificial far-away boundary to simulate the Honein's unbounded problem under the remote shear. The stress $\sigma_{rz}$ applied on the artificial boundary is equivalent to the Neumann boundary condition

$$\frac{\partial w}{\partial \mathbf{n}} = \nabla w \cdot \mathbf{n} = \frac{1}{\mu}\sigma_{rz} = \frac{1}{\mu}\sin\theta \quad \text{on} \quad B_0 \tag{14}$$

where $B_0$ is the artificial far-away boundary bounded by a circle of radius $R_0$. For all the inner boundaries, traction-free conditions for $\frac{\partial w}{\partial n}$ instead of Eq. (11) are specified. Not only the equivalent stress [3] but also the equivalent displacement in the present paper on the artificial boundary are alternatives to solving the problems by using the bounded-domain approach in place of the infinite plane where $w(x, y)|_{(x,y)\in R_0} = R_0 \sin\theta$. In the following cases, only Case 3 is solved by the equivalent displacement and stress approaches.

## 3. Solution procedures

### 3.1. Dual boundary integral equations and dual null-field integral equations

We apply the Fourier series expansions to approximate the potential $w^s$ and its normal derivative on the boundary

$$w^s(s_k) = a_0^k + \sum_{n=1}^{\infty}(a_n^k \cos n\theta_k + b_n^k \sin n\theta_k), \quad \times \quad s_k \in B_k, \quad k = 1,2,\cdots,N, \tag{15}$$

$$t^s(s_k) = p_0^k + \sum_{n=1}^{\infty}(p_n^k \cos n\theta_k + q_n^k \sin n\theta_k), \quad \times \quad s_k \in B_k, \quad k = 1,2,\cdots,N, \tag{16}$$

where $t^s(s_k)=\frac{\partial w^s(s_k)}{\partial n_s}$, $a_n^k$, $b_n^k$, $p_n^k$ and $q_n^k$ ($n=0, 1, 2, \ldots$) are the Fourier coefficients and $\theta_k$ is the polar angle. The integral equation for the domain point can be derived from the third Green's identity [5], we have

$$2\pi w^s(x) = \int_B T(s,x)w^s(s)\mathrm{d}B(s) - \int_B U(s,x)t^s(s)\mathrm{d}B(s), \quad x \in D, \tag{17}$$

$$2\pi \frac{\partial w^s(x)}{\partial \mathbf{n}_x} = \int_B M(s,x)w^s(s)\mathrm{d}B(s) - \int_B L(s,x)t^s(s)\mathrm{d}B(s), \quad x \in D, \tag{18}$$

where s and x are the source and field points, respectively, $B$ is the boundary, $D$ is the domain of interest, $\mathbf{n}_s$ and $\mathbf{n}_x$ denote the outward normal vector at the source point s and field point x, respectively, and the kernel function $U(\mathrm{s,x})=\ln r$, ($r \equiv |\mathrm{x\text{-}s}|$), is the fundamental solution which satisfies

$$\nabla^2 U(s,x) = 2\pi\delta(x-s), \tag{19}$$

in which $\delta$ (x-s) denotes the Dirac-delta function. The other kernel functions, $T$ (s, x), $L$ (s, x) and $M$ (s, x), are defined by

$$T(\mathrm{s,x}) \equiv \frac{\partial U(\mathrm{s,x})}{\partial \mathbf{n}_s}, \quad L(\mathrm{s,x}) \equiv \frac{\partial U(\mathrm{s,x})}{\partial \mathbf{n}_x}, \quad M(\mathrm{s,x}) \equiv \frac{\partial^2 U(\mathrm{s,x})}{\partial \mathbf{n}_s \partial \mathbf{n}_x}, \tag{20}$$

By collocating x outside the domain ($\mathrm{x} \in D^c$), we obtain the dual null-field integral equations as shown below

$$0 = \int_B T(\mathrm{s,x})w^s(\mathrm{s})\mathrm{d}B(\mathrm{s}) - \int_B U(\mathrm{s,x})t^s(\mathrm{s})\mathrm{d}B(\mathrm{s}), \quad \mathrm{x} \in D^c, \tag{21}$$

$$0 = \int_B M(\mathrm{s,x})w^s(\mathrm{s})\mathrm{d}B(\mathrm{s}) - \int_B L(\mathrm{s,x})t^s(\mathrm{s})\mathrm{d}B(\mathrm{s}), \quad \mathrm{x} \in D^c, \tag{22}$$

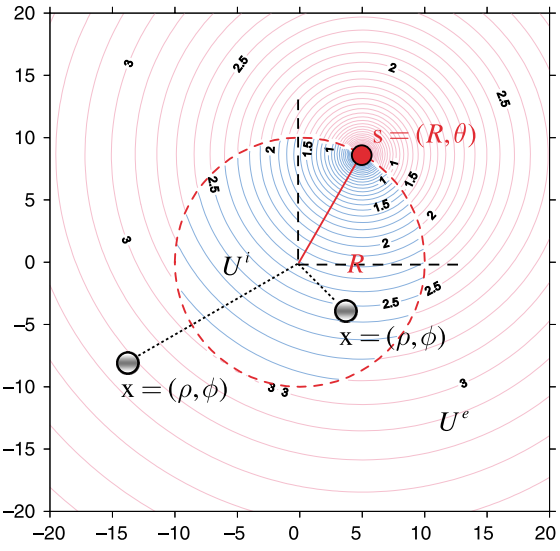


Fig. 3. Graph of the separate expression of fundamental solution where the source s located at $R=10.0$ and $\theta=\pi/3$.

where $D^c$ is the complementary domain. Based on the separable property, the kernel function $U$(s, x) can be expanded into degenerate form by separating the source points and field points in the polar coordinate [6]:

$$U(\mathrm{s,x}) = \begin{cases} U^i(R,\theta;\rho,\phi) = \ln R - \sum_{m=1}^{\infty}\frac{1}{m}\left(\frac{\rho}{R}\right)^m \cos m(\theta-\phi), & R \geq \rho \\ U^e(R,\theta;\rho,\phi) = \ln \rho - \sum_{m=1}^{\infty}\frac{1}{m}\left(\frac{R}{\rho}\right)^m \cos m(\theta-\phi), & \rho > R \end{cases}, \tag{23}$$

where the superscripts "$i$" and "$e$" denote the interior ($R>\rho$) and exterior ($\rho>R$) cases, respectively. The origin of the observer system for the degenerate kernel is (0, 0). Fig. 3 shows the graph of separate expressions of fundamental solutions where source point s located at $R=10.0$, $\theta=\pi/3$. By setting the origin at $o$ for the observer system, a circle with radius $R$ from the origin $o$ to the source point s is plotted. If the field point x is situated inside the circular region, the degenerate kernel belongs to the interior case $U^i$; otherwise, it is the exterior case. After taking the normal derivative with respect to Eq. (23), the $T$(s, x) kernel can be derived as

$$T(\mathrm{s,x}) = \begin{cases} T^i(R,\theta;\rho,\phi) = \frac{1}{R} + \sum_{m=1}^{\infty}\left(\frac{\rho^m}{R^{m+1}}\right)\cos m(\theta-\phi), & R > \rho \\ T^e(R,\theta;\rho,\phi) = -\sum_{m=1}^{\infty}\left(\frac{R^{m-1}}{\rho^m}\right)\cos m(\theta-\phi), & \rho > R \end{cases}, \tag{24}$$

and the higher-order kernel functions, $L$(s, x) and $M$(s, x), are shown below

$$L(\mathrm{s},\mathrm{x}) = \begin{cases} L^i(R,\theta;\rho,\phi) = -\sum_{m=1}^{\infty}\left(\frac{\rho^{m-1}}{R^m}\right)\cos m(\theta-\phi), & R>\rho \\ L^e(R,\theta;\rho,\phi) = \frac{1}{\rho}+\sum_{m=1}^{\infty}\left(\frac{R^m}{\rho^{m+1}}\right)\cos m(\theta-\phi), & \rho>R \end{cases}, \tag{25}$$

$$M(\mathrm{s},\mathrm{x}) = \begin{cases} M^i(R,\theta;\rho,\phi) = \sum_{m=1}^{\infty}\left(\frac{m\rho^{m-1}}{R^{m+1}}\right)\cos m(\theta-\phi), & R\geq\rho \\ M^e(R,\theta;\rho,\phi) = \sum_{m=1}^{\infty}\left(\frac{mR^{m-1}}{\rho^{m+1}}\right)\cos m(\theta-\phi), & \rho>R \end{cases}. \tag{26}$$

Since the potential resulted from $T(\mathrm{s},\mathrm{x})$ and $L(\mathrm{s},\mathrm{x})$ kernels are discontinuous cross the boundary, the potentials of $T(\mathrm{s},\mathrm{x})$ for $R\to\rho^+$ and $R\to\rho^-$ are different. This is the reason why $R=\rho$ is not included in expressional degenerate kernels of $T(\mathrm{s},\mathrm{x})$ and $L(\mathrm{s},\mathrm{x})$ in Eqs. (24) and (25).

### 3.2. Adaptive observer system

After collocating points in the null-field integral equation of Eq. (21), the boundary integrals through all the circular contours are required. Since the boundary integral equations are frame indifferent, *i.e.* objectivity rule, the observer system is adaptively to locate the origin at the center of circle in the boundary integrals. Adaptive observer system is chosen to fully employ the property of degenerate kernels. Fig. 4 (a) and (b) show the boundary integration for the circular boundaries in the adaptive observer system. It is worthy noted that the origin of the observer system is located on the center of the corresponding circle under integration to entirely utilize the geometry of circular boundary for the expansion of degenerate kernels and boundary densities. The dummy variable in the circular integration is angle ($\theta$) instead of radial coordinate ($R$).

### 3.3. Linear algebraic system

By moving the null-field point $\mathrm{x}_j$ to the *jth* circular boundary in the limit sense for Eq. (21) in Fig. 4(a), we have

$$0 = \sum_{k=0}^{N}\int_{B_k} T^i(R,\theta;\rho_j,\phi_j)w^s(R,\theta)\mathrm{d}B_k(R,\theta) - \sum_{k=0}^{N}\int_{B_k} U^i(R,\theta;\rho_j,\phi_j)t^s(R,\theta)\mathrm{d}B_k(R,\theta), \quad \mathrm{x}(\rho_j,\phi_j)\in D^c, \tag{27}$$

where $N$ is the number of inner circular holes. If the domain is unbounded, the outer boundary $B_0$ is a null set. Note that the kernels $U^i$ and $T^i$ are assumed in the degenerate form given by Eqs. (23) and (24), respectively while the boundary densities $w^s$ and $t^s$ are applied in the Fourier series expansion forms given by Eqs. (15) and (16), respectively. Then, the integrals multiplied by separate expansion coefficients in Eq. (27) are non-singular and the limit of the null-field point to the boundary is trivial. Thus, the collocation point $\mathrm{x}(\rho_j, \phi_j)$ in the discretized Eq. (27) can be considered on the boundary $B_j$, too. In contrast to the standard discretized BIE formulation with nodal unknowns of the physical boundary densities $w^s$ and $t^s$, now the degrees of freedom are given by coefficients employed in the Fourier expansions of these densities. It is found that the compatible relationship of the boundary unknowns is equivalent by moving either the domain point or the null-field point to the boundary in different directions. For clarity, we design a simple case of 2-D circular region to demonstrate the validity of the present formulation in Appendix A. It is noted that the integration path is counterclockwise for the outer circle. Otherwise, it is clockwise. In the $B_k$ integration, we set the origin of the observer system to collocate at the center $c_k$ to fully utilize the degenerate kernels and Fourier series. By collocating the null-field point on the boundary, a linear algebraic system is obtained

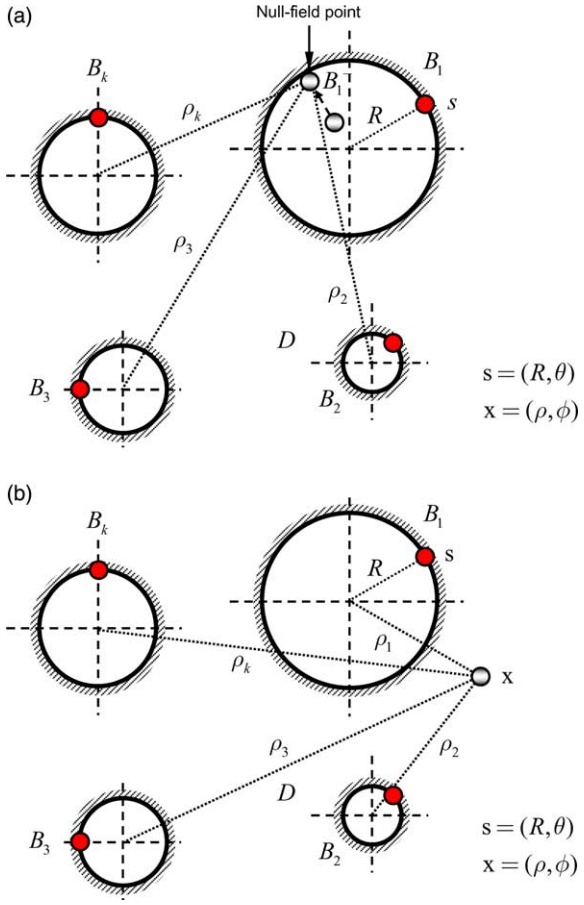


Fig. 4. (a) Sketch of the null-field integral equation in conjunction with the adaptive observer system, (b) Sketch of the boundary integral equation for domain points in conjunction with the adaptive observer system.

$$[\mathbf{U}]\{\mathbf{t}^s\} = [\mathbf{T}]\{\mathbf{w}^s\}, \tag{28}$$

where $[\mathbf{U}]$ and $[\mathbf{T}]$ are the influence matrices with a dimension of $(N+1)(2M+1)$ by $(N+1)(2M+1)$, $\{\mathbf{w}^s\}$ and $\{\mathbf{t}^s\}$ denote the

Table 1
Comparisons of the present method and conventional BEM

| Boundary density discretization | Auxiliary system | Formulation | Observer system | Singularity |
|---|---|---|---|---|
| Fourier series 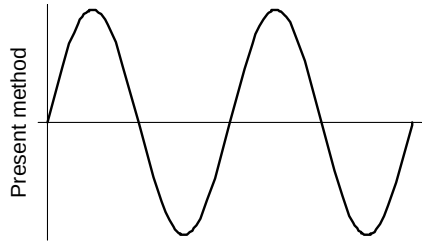  | Degenerate kernel | Null-field integral equation | Adaptive observer system | No principal value |
| Constant element 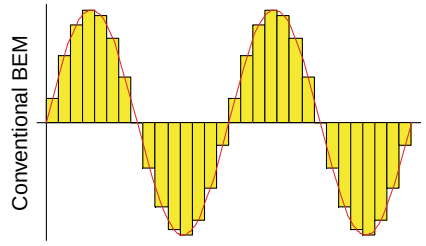  | Fundamental solution | Boundary integral equation | Fixed observer system | Principal value (*C.P.V.*, *R.P.V.* and *H.P.V.*) |

where *C.P.V.*, *R.P.V.* and *H.P.V.* are the Cauchy principal value, Riemann principal value and Hadamard principal value, respectively

column vectors of Fourier coefficients with a dimension of $(N+1)(2M+1)$ by 1 in which $[\mathbf{U}]$, $[\mathbf{T}]$, $\{\mathbf{w}^s\}$ and $\{\mathbf{t}^s\}$ can be defined as follows:

$$[\mathbf{U}] = \begin{bmatrix} \mathbf{U}_{00} & \mathbf{U}_{01} & \cdots & \mathbf{U}_{0N} \\ \mathbf{U}_{10} & \mathbf{U}_{11} & \cdots & \mathbf{U}_{1N} \\ \vdots & \vdots & \ddots & \vdots \\ \mathbf{U}_{N0} & \mathbf{U}_{N1} & \cdots & \mathbf{U}_{NN} \end{bmatrix}, \quad [\mathbf{T}] = \begin{bmatrix} \mathbf{T}_{00} & \mathbf{T}_{01} & \cdots & \mathbf{T}_{0N} \\ \mathbf{T}_{10} & \mathbf{T}_{11} & \cdots & \mathbf{T}_{1N} \\ \vdots & \vdots & \ddots & \vdots \\ \mathbf{T}_{N0} & \mathbf{T}_{N1} & \cdots & \mathbf{T}_{NN} \end{bmatrix}, \tag{29}$$

$$\{\mathbf{w}^s\} = \begin{Bmatrix} \mathbf{w}_0^s \\ \mathbf{w}_1^s \\ \mathbf{w}_2^s \\ \vdots \\ \mathbf{w}_N^s \end{Bmatrix}, \quad \{\mathbf{t}^s\} = \begin{Bmatrix} \mathbf{t}_0^s \\ \mathbf{t}_1^s \\ \mathbf{t}_2^s \\ \vdots \\ \mathbf{t}_N^s \end{Bmatrix}, \tag{30}$$

where the vectors $\{\mathbf{w}_k^s\}$ and $\{\mathbf{t}_k^s\}$ are in the form of $\{a_0^k \ a_1^k \ b_1^k \ \cdots \ a_M^k \ b_M^k\}^T$ and $\{p_0^k \ p_1^k \ q_1^k \ \cdots \ p_M^k \ q_M^k\}^T$, respectively; the first subscript "$j$" ($j=0, 1, 2, \ldots N$) in $[\mathbf{U}_{jk}]$ and $[\mathbf{T}_{jk}]$ denotes the index of the *jth* circle where the collocation point is located and the second subscript "$k$" ($k=0, 1, 2, \ldots N$) denotes the index of the *kth* circle where boundary data $\{\mathbf{w}_k^s\}$ or $\{\mathbf{t}_k^s\}$ are specified, $N$ is the number of circular holes in the domain and $M$ indicates the truncated terms of Fourier series. The coefficient matrix of the linear algebraic system is partitioned into blocks, and each off-diagonal block corresponds to the influence matrices between two different circular cavities. The diagonal blocks are the influence matrices due to itself in each individual hole. After uniformly collocating the point along the *kth* circular boundary, the submatrix can be written as

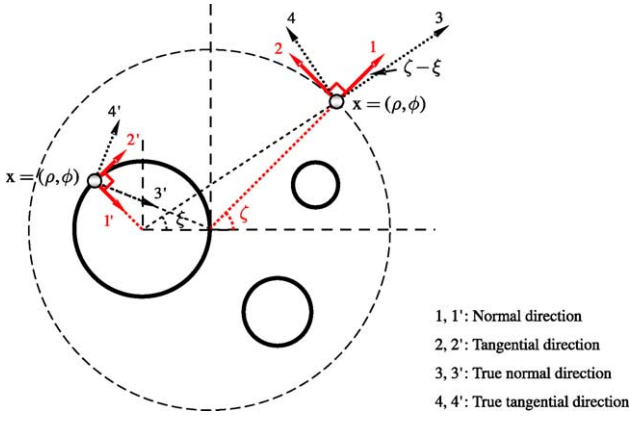


Fig. 5. Vector decomposition for the potential gradient in the hypersingular equation.

$$[\mathbf{U}_{jk}] = \begin{bmatrix} U_{jk}^{0c}(\phi_1) & U_{jk}^{1c}(\phi_1) & U_{jk}^{1s}(\phi_1) & \cdots & U_{jk}^{Mc}(\phi_1) & U_{jk}^{Ms}(\phi_1) \\ U_{jk}^{0c}(\phi_2) & U_{jk}^{1c}(\phi_2) & U_{jk}^{1s}(\phi_2) & \cdots & U_{jk}^{Mc}(\phi_2) & U_{jk}^{Ms}(\phi_2) \\ U_{jk}^{0c}(\phi_3) & U_{jk}^{1c}(\phi_3) & U_{jk}^{1s}(\phi_3) & \cdots & U_{jk}^{Mc}(\phi_3) & U_{jk}^{Ms}(\phi_3) \\ \vdots & \vdots & \vdots & \ddots & \vdots & \vdots \\ U_{jk}^{0c}(\phi_{2M}) & U_{jk}^{1c}(\phi_{2M}) & U_{jk}^{1s}(\phi_{2M}) & \cdots & U_{jk}^{Mc}(\phi_{2M}) & U_{jk}^{Ms}(\phi_{2M}) \\ U_{jk}^{0c}(\phi_{2M+1}) & U_{jk}^{1c}(\phi_{2M+1}) & U_{jk}^{1s}(\phi_{2M+1}) & \cdots & U_{jk}^{Mc}(\phi_{2M+1}) & U_{jk}^{Ms}(\phi_{2M+1}) \end{bmatrix}, \tag{31}$$

$$[\mathbf{T}_{jk}] = \begin{bmatrix} T_{jk}^{0c}(\phi_1) & T_{jk}^{1c}(\phi_1) & T_{jk}^{1s}(\phi_1) & \cdots & T_{jk}^{Mc}(\phi_1) & T_{jk}^{Ms}(\phi_1) \\ T_{jk}^{0c}(\phi_2) & T_{jk}^{1c}(\phi_2) & T_{jk}^{1s}(\phi_2) & \cdots & T_{jk}^{Mc}(\phi_2) & T_{jk}^{Ms}(\phi_2) \\ T_{jk}^{0c}(\phi_3) & T_{jk}^{1c}(\phi_3) & T_{jk}^{1s}(\phi_3) & \cdots & T_{jk}^{Mc}(\phi_3) & T_{jk}^{Ms}(\phi_3) \\ \vdots & \vdots & \vdots & \ddots & \vdots & \vdots \\ T_{jk}^{0c}(\phi_{2M}) & T_{jk}^{1c}(\phi_{2M}) & T_{jk}^{1s}(\phi_{2M}) & \cdots & T_{jk}^{Mc}(\phi_{2M}) & T_{jk}^{Ms}(\phi_{2M}) \\ T_{jk}^{0c}(\phi_{2M+1}) & T_{jk}^{1c}(\phi_{2M+1}) & T_{jk}^{1s}(\phi_{2M+1}) & \cdots & T_{jk}^{Mc}(\phi_{2M+1}) & T_{jk}^{Ms}(\phi_{2M+1}) \end{bmatrix}. \tag{32}$$

Although both the matrices in Eqs. (31) and (32) are not sparse, it is found that the higher order harmonics, the lower influence coefficients in numerical experiments. It is noted that the superscript "0s" in Eqs. (31) and (32) disappears since sin $(\theta)=0$. The element of $[\mathbf{U}_{jk}]$ and $[\mathbf{T}_{jk}]$ are defined respectively as

$$U_{jk}^{nc}(\phi_m) = \int_{B_k} U(\mathrm{s}_k, \mathrm{x}_m)\cos(n\theta_k)R_k \mathrm{d}\theta_k, \quad n = 0, 1, 2, \cdots, M, \quad m = 1, 2, \cdots, 2m+1, \tag{33}$$

$$U_{jk}^{ns}(\phi_m) = \int_{B_k} U(\mathrm{s}_k, \mathrm{x}_m)\sin(n\theta_k)R_k \mathrm{d}\theta_k, \quad n = 1, 2, \cdots, M, \quad m = 1, 2, \cdots, 2M+1, \tag{34}$$

$$T_{jk}^{ns}(\phi_m) = \int_{B_k} T(\mathrm{s}_k, \mathrm{x}_m)\cos(n\theta_k)R_k \mathrm{d}\theta_k, \quad n = 0, 1, 2, \cdots, M, \quad m = 1, 2, \cdots, 2M+1, \tag{35}$$

$$T_{jk}^{ns}(\phi_m) = \int_{B_k} T(\mathrm{s}_k, \mathrm{x}_m)\sin(n\theta_k)R_k \mathrm{d}\theta_k, \quad n = 1, 2, \cdots, M, \quad m = 1, 2, \cdots, 2M+1, \tag{36}$$

where $k$ is no sum and $\phi_m$ is the polar angle of the collocating points $\mathrm{x}_m$ along the boundary. By rearranging the known and unknown sets, the unknown Fourier coefficients are determined. Eq. (21) can be calculated by employing the relations of trigonometric function and the orthogonal property in the real computation. Only the finite $M$ terms are used in the summation of Eqs. (15) and (16). After obtaining the unknown Fourier coefficients, the origin of observer system is set to $c_k$ in the $B_k$ integration as shown in Fig. 4 (b) to obtain the interior potential by employing Eq. (17). The differences between the present formulation and the conventional BEM are listed in Table 1.

### 3.4. Vector decomposition technique for the potential gradient in hypersingular equation

Eq. (18) shows the normal derivative of potential for domain points, special treatment is considered here. Potential gradient on the boundary is required to calculate for $\sigma_{\theta z}$. For the nonconcentric cavities, special treatment for the potential gradient should be taken care as the source point and field point locate on different circular boundaries. As shown in Fig. 5, the normal direction on the boundary (1, 1') should be superimposed by the radial derivative (3, 3') and angular derivative (4, 4'). We called this treatment "vector decomposition technique". According to the concept of vector decomposition technique, Eqs. (25) and (26) can be modified to

$$L(\mathrm{s},\mathrm{x}) = \begin{cases} L^i(R,\theta;\rho,\phi) = -\sum_{m=1}^{\infty}\left(\frac{\rho^{m-1}}{R^m}\right)\cos m(\theta-\phi)\cos(\zeta-\xi) - \sum_{m=1}^{\infty}\left(\frac{\rho^{m-1}}{R^m}\right)\sin m(\theta-\phi)\cos\left(\frac{\pi}{2}-\zeta+\xi\right), & R>\rho \\ L^e(R,\theta;\rho,\phi) = \frac{1}{\rho} + \sum_{m=1}^{\infty}\left(\frac{R^m}{\rho^{m+1}}\right)\cos m(\theta-\phi)\cos(\zeta-\xi) - \sum_{m=1}^{\infty}\left(\frac{R^m}{\rho^{m+1}}\right)\sin m(\theta-\phi)\cos\left(\frac{\pi}{2}-\zeta+\xi\right), & \rho>R \end{cases}, \tag{37}$$

$$M(\mathrm{s},\mathrm{x}) = \begin{cases} M^i(R,\theta;\rho,\phi) = \sum_{m=1}^{\infty}\left(\frac{m\rho^{m-1}}{R^{m+1}}\right)\cos m(\theta-\phi)\cos(\zeta-\xi) - \sum_{m=1}^{\infty}\left(\frac{m\rho^{m-1}}{R^{m+1}}\right)\sin m(\theta-\phi)\cos\left(\frac{\pi}{2}-\zeta+\xi\right), & R\geq\rho \\ M^e(R,\theta;\rho,\phi) = \sum_{m=1}^{\infty}\left(\frac{mR^{m-1}}{\rho^{m+1}}\right)\cos m(\theta-\phi)\cos(\zeta-\xi) - \sum_{m=1}^{\infty}\left(\frac{mR^{m-1}}{\rho^{m+1}}\right)\sin m(\theta-\phi)\cos\left(\frac{\pi}{2}-\zeta+\xi\right), & \rho>R \end{cases}, \quad (38)$$

where $\zeta$ and $\xi$ are shown in Fig. 5. For the special case, the circles with respect to the same origin of observer, the potential gradient is derived free of special treatment since $\zeta=\xi$.

## 4. Illustrative examples and discussions

What is being discussed here are the problems of two circular cavities, whose centers lie on the line joining the two centers making 45 degrees and touch each other solved by Honein *et al.*. All the numerical results are given below by using the twenty terms of Fourier series ($M=20$) except for Case 2 of interacting cavities. The extension to three holes is also conducted.

Case 1: Two circular holes lie on the line joining the two centers making 45 degrees

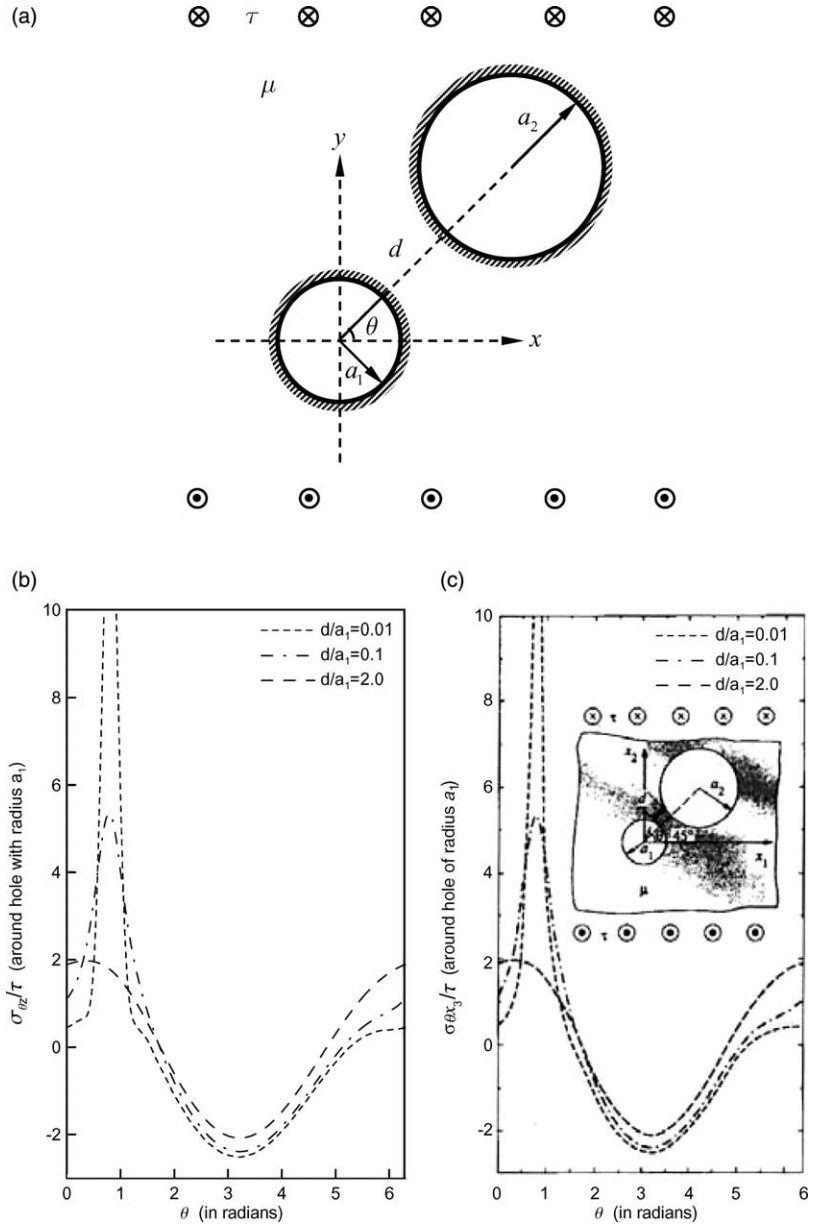


Fig. 6. (a) Two circular holes with centers on the line making 45 degrees, (b) $\sigma_{\theta z}$ around the hole of radius $a_1$, (c) Honein's data [11].

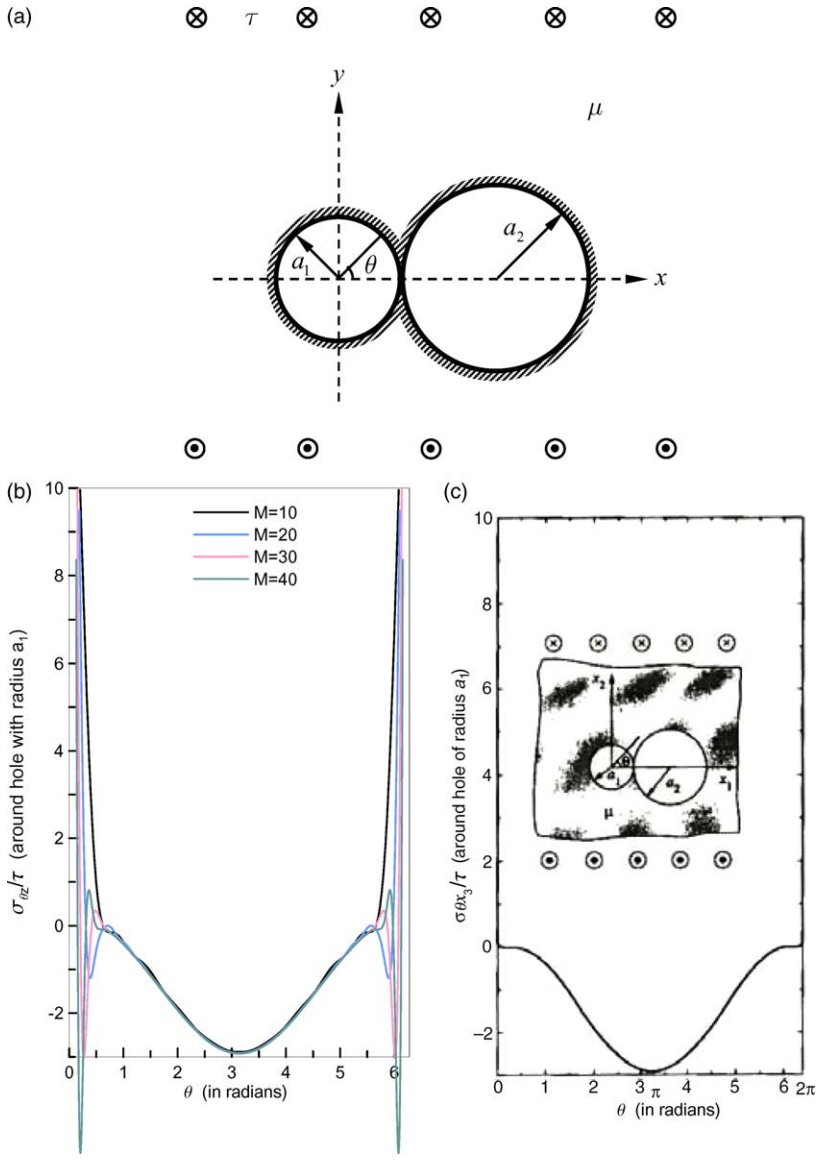


Fig. 7. (a) Two circular holes touching each other, (b) $\sigma_{\theta z}$ around the hole of radius $a_1$, (c) Honein's data [11].

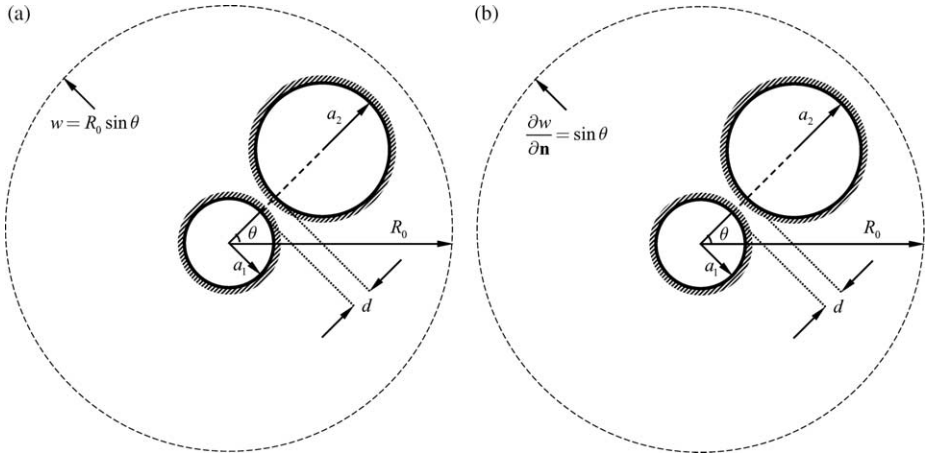


Fig. 8. (a) A bounded-domain approach using equivalent displacement applied on the remote boundary of radius $R_0$, (b) A bounded-domain approach using equivalent stress applied on the remote boundary of radius $R_0$. (c) $\sigma_{\theta z}$ around the hole of radius $a_1$ using equivalent stress approach, (d) Steele's data [3], (e) $\sigma_{\theta z}$ around the hole of radius $a_1$ using equivalent displacement approach, (f) Honein's data [11], (g) Convergence rate of stress $\sigma_{\theta z}$ at $\theta = 45°$ versus $R_0$ in the equivalent displacement and stress approaches.

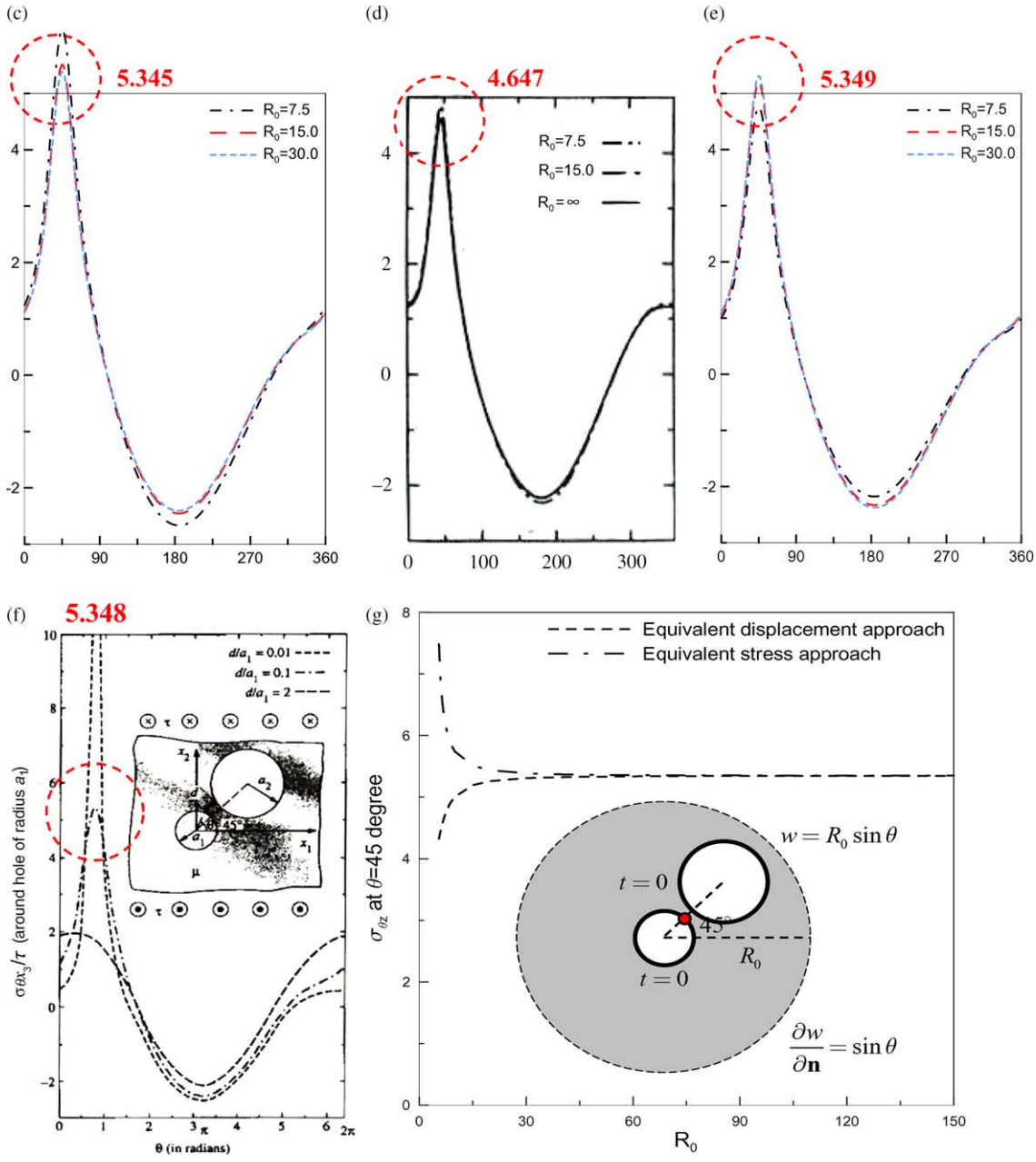


Fig. 8 (*continued*)

Figure 6 (a) shows the geometry of the two circles whose radii are $a_1$ and $a_2$ ($a_2=2a_1$). In Fig. 6 (b), the maximum stress appears at $\theta=\pi/4$ as the holes are close to each other on the line joining their centers. Our numerical results are compared with the data of Honein's results in Fig. 6 (c), good agreement can be obtained.

Case 2: Two circular holes touching each other

The case of two holes touching each other is treated as Case 2 as shown in Fig. 7 (a). Figures 7 (b) and (c) show the graphs of stress field around the circle centered at the origin. We see that the stress is infinite at the neighbor point of the two circles. Figure 7 (b) shows our solution by using different terms ($M=$ 10, 20, 30, 40). It is worthy noted that our data agree well with the Honein's data except the intersecting point as the numbers of terms increases. Physically speaking, the geometry of the two circles is like a peanut and the shear stress at $\theta=0^+$ and $\theta=2\pi^-$ is discontinuous. However, the stresses at the closest points have impulses due to the fact that they are continuous when using the present method.

Case 3: Two equivalent bounded-domain approaches with specified displacement or stress on the remote circular boundary

The concept of equivalent bounded-domain approach to approximating the results of infinite problems was reported in Bird and Steele's paper [3] by using the stress approach. Here, the displacement approach as well as the stress approach is considered as shown in Fig. 8 (a) and (b), respectively. Figure 8 (c) shows $\sigma_{\theta z}$ along the boundary of small circle with the

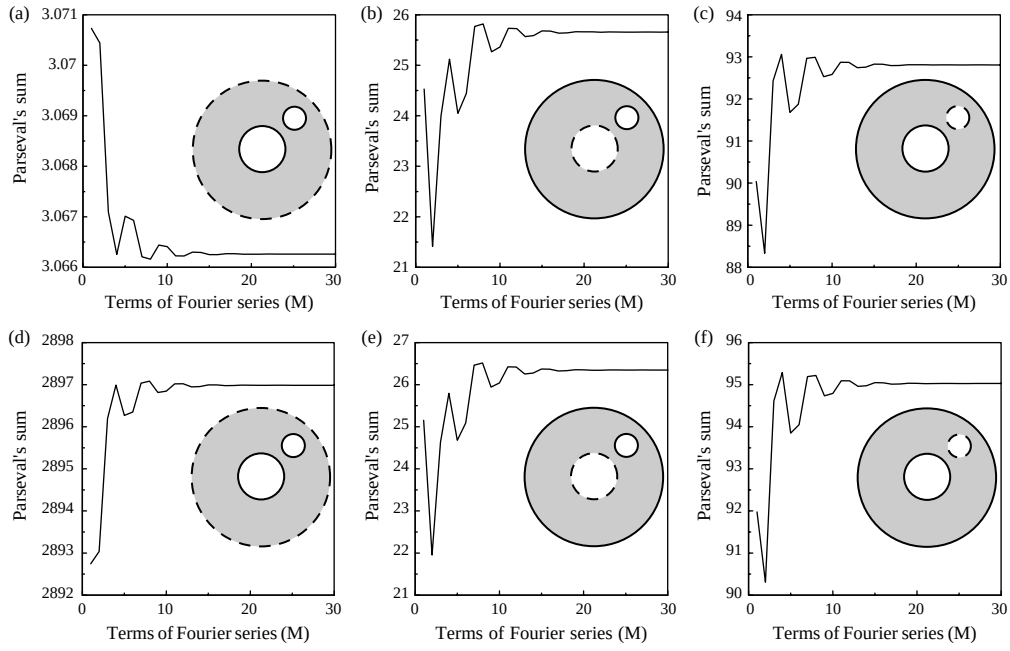


Fig. 9. (a) Parseval's sum for the outer circle using the displacement approach, (b) Parseval's sum for the circle of radius $a_1$ using the displacement approach, (c) Parseval's sum for the circle of radius $a_2$ using the displacement approach, (d) Parseval's sum for the outer circle using the stress approach, (e) Parseval's sum for the circle of radius $a_1$ using the stress approach, (f) Parseval's sum for the circle of radius $a_2$ using the stress approach.

equivalent stress which is applied on the remote circular boundary. The results better match the Honein's solutions than those of Bird and Steele in Fig. 8 (d). Furthermore, the displacement approach works well as shown in Fig. 8 (e). It is quite clear to see that the results for the radius of the outer boundary $R_0=30.0$ agree very well with those resulting from infinite plane investigated by Honein *et al.* in Fig. 8 (f). The relative error at $\theta=\pi/4$ of Bird and Steele's data ($>13\%$) is greater than any one of our solution ($<1\%$) using either displacement or stress approach. The convergence of the stress $\sigma_{\theta z}$ versus the outer radius $R_0$ is plotted in Fig. 8 (g). It is interesting to find that both the two approaches converge to the Honein's solution of infinite domain in opposite directions. It can be explained that the displacement approach makes the system stiffer and these results in the upper bound solution. On the other hand, the stress approach makes the system more flexible, so we obtain the lower bound solution. Nevertheless, they converge to the same solution. Furthermore, we adopted the Parseval's sum to examine how many terms of Fourier series are required for

$$\int_0^{2\pi} [w^s(\theta)]^2 \mathrm{d}\theta \doteq 2\pi a_0^2 + \pi \sum_{n=1}^{M} (a_n^2 + b_n^2). \tag{39}$$

According to Eq. (39), we plotted the Parseval's sum versus M (numbers of Fourier series) for each circle by using displacement and stress approaches in Fig. 9 (a)–(f), respectively. It indicates that twenty terms are required.

Case 4: Three circular holes lie on the line joining the centers making 45 degrees

Fig. 10 (a) shows the positions of the three holes. In Fig. 10 (b), the stress $\sigma_{\theta z}$ on the hole of radius $a_1$ at the closest points becomes larger as the distance $d$ is very small.

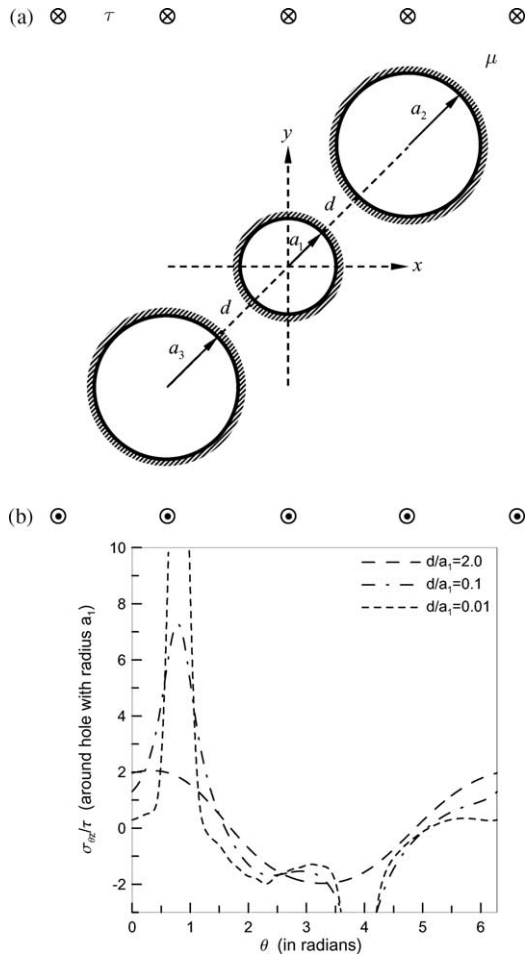


Fig. 10. (a) Three circular holes with centers on the line making 45 degrees, (b) $\sigma_{\theta z}$ around the hole of radius $a_1$ using the present formulation.

## 5. Conclusions

A semi-analytical formulation for multiple arbitrary circular holes using degenerate kernels and Fourier series in an adaptive observer system was developed. The singularity and hypersingularity were avoided after introducing the concept of degenerate kernels. Two examples with two circular holes investigated by Honein *et al.* were revisited. Furthermore, the bounded-domain approaches using either the equivalent displacement or equivalent stress were proposed. Good agreements were made after comparing with the Honein's data. Regardless of the number of circles, the proposed method can offer good results. The three-hole problem was successfully demonstrated to see the validity of the present method. The "semi-analytical" result of three-cavity problem may provide a datum for comparison when other numerical methods are used. Moreover, our method presented here can be applied to circular problems which satisfy the Laplace equation.

## Appendix A

To demonstrate the validity of the present formulation, the compatible relationship of the boundary data can be derived in two ways by moving the point to the boundary. One is from the boundary integral equation for the domain point. The other is the null-field integral equation. By moving either the domain point or the null-field point to the boundary in the different directions, we will prove the equivalence for the compatible relationship of the boundary data. A 2-D case is considered below.

The 2-D circular region is shown in Fig. 11. First, we use the null-field integral equation of Eq. (27) to determine the unknown boundary data. By moving x to the boundary of $\rho = 1^+$ and substituting the appropriate degenerate kernels in Eqs. (23) and (24) into Eq. (27), we have

$$\begin{bmatrix} 0 & 0 & 0 & \cdots & 0 & 0 \\ 0 & \pi\cos\phi & 0 & \cdots & 0 & 0 \\ 0 & 0 & \pi\sin\phi & \cdots & 0 & 0 \\ \vdots & \vdots & \vdots & \ddots & \vdots & \vdots \\ 0 & 0 & 0 & \cdots & \pi\cos m\phi & 0 \\ 0 & 0 & 0 & \cdots & 0 & \pi\sin m\phi \end{bmatrix} \begin{Bmatrix} a_0 \\ a_1 \\ b_1 \\ \vdots \\ a_m \\ b_m \end{Bmatrix} = \begin{bmatrix} 2\pi\ln 1 & 0 & 0 & \cdots & 0 & 0 \\ 0 & \pi\cos\phi & 0 & \cdots & 0 & 0 \\ 0 & 0 & \pi\sin\phi & \cdots & 0 & 0 \\ \vdots & \vdots & \vdots & \ddots & \vdots & \vdots \\ 0 & 0 & 0 & \cdots & \frac{\pi}{m}\cos m\phi & 0 \\ 0 & 0 & 0 & \cdots & 0 & \frac{\pi}{m}\sin m\phi \end{bmatrix} \begin{Bmatrix} p_0 \\ p_1 \\ q_1 \\ \vdots \\ p_m \\ q_m \end{Bmatrix}. \tag{A1}$$

Similarly, we move the domain point in Eq. (17) to the boundary of $\rho = 1^-$ and employ the appropriate degenerate kernels. We obtain

$$\begin{bmatrix} 2\pi-2\pi & 0 & 0 & \cdots & 0 & 0 \\ 0 & (2\pi-\pi)\cos\phi & 0 & \cdots & 0 & 0 \\ 0 & 0 & (2\pi-\pi)\sin\phi & \cdots & 0 & 0 \\ \vdots & \vdots & \vdots & \ddots & \vdots & \vdots \\ 0 & 0 & 0 & \cdots & (2\pi-\pi)\cos m\phi & 0 \\ 0 & 0 & 0 & \cdots & 0 & (2\pi-\pi)\sin m\phi \end{bmatrix} \begin{Bmatrix} a_0 \\ a_1 \\ b_1 \\ \vdots \\ a_m \\ b_m \end{Bmatrix} = \begin{bmatrix} 2\pi\ln 1 & 0 & 0 & \cdots & 0 & 0 \\ 0 & \pi\cos\phi & 0 & \cdots & 0 & 0 \\ 0 & 0 & \pi\sin\phi & \cdots & 0 & 0 \\ \vdots & \vdots & \vdots & \ddots & \vdots & \vdots \\ 0 & 0 & 0 & \cdots & \frac{\pi}{m}\cos m\phi & 0 \\ 0 & 0 & 0 & \cdots & 0 & \frac{\pi}{m}\sin m\phi \end{bmatrix} \begin{Bmatrix} p_0 \\ p_1 \\ q_1 \\ \vdots \\ p_m \\ q_m \end{Bmatrix}. \tag{A2}$$

Both Eqs. (A1) and (A2) are found be the same. In the real implenentation, we select the null-field integral since the diagonal terms of Eq. (A1) is more simple than those of Eq. (A2). It is noted that the singular matrices in Eqs. (A1)

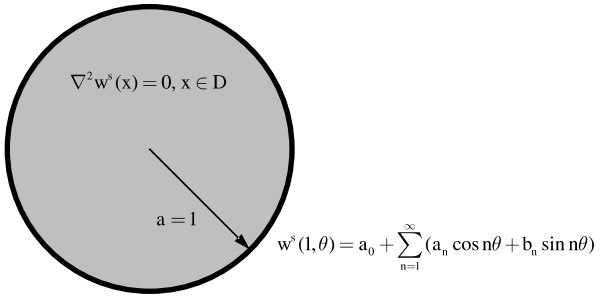


Fig. 11. Laplace problem in 2-D region.

and (A2) can be explained as the rigid body solution for the Neumann problem and the degenerate scale (so called logarithmic capacity) for the Dirichelet problem.

## References

[1] Ang WT, Kang I. A complex variable boundary element method for elliptic partial differential equations in a multiply-connected region. Int J Comput Math 2000;75:515–25.
[2] Ang WT. Private communication; 2005.
[3] Bird MD, Steele CR. A solution procedure for Laplace's equation on multiply-connected circular domains. ASME J Appl Mech 1992;59: 398–404.
[4] Chen JT, Hong H-K. Boundary element method. Taipei Taiwan: New World Press; 1992.
[5] Chen JT, Hong H-K. Review of dual boundary element methods with emphasis on hypersingular integrals and divergent series. ASME Appl Mech Rev 1999;52:17–33.
[6] Chen JT, Chiu YP. On the pseudo-differential operators in the dual boundary integral equations using degenerate kernels and circulants. Eng Anal Bound Elem 2002;26:41–53.
[7] Chou SI. Stress field around holes in antiplane shear using complex variable boundary element method. ASME J Appl Mech 1997;64: 432–5.
[8] Gray LJ, Manne LL. Hypersingular integrals at a corner. Eng Anal Bound Elem 1993;11:327–34.
[9] Guiggiani M. Hypersingular boundary integral equations have an additional free term. Comput Mech 1995;16:245–8.
[10] Honein E, Honein T, Herrmann G. Further aspects of the elastic field for two circular inclusions in antiplane elastostatics. ASME J Appl Mech 1992;59:774–9.
[11] Honein E, Honein T, Herrmann G. On two circular inclusions in harmonic problems. Q Appl Math 1992;50:479–99.
[12] Honein E, Honein T, Herrmann G. Energetics of two circular inclusions in anti-plane elastostatics. Int J Solids Struct 2000;37:3667–79.
[13] Hromadka TV, Lai C. The complex variable boundary element method in engineering analysis. New York: Springer–Verlag; 1986.
[14] Mogilevskaya SG, Crouch SL. A Galerkin boundary integral method for multiple circular elastic inclusions. Int J Numer Meth Eng 2001;52: 1069–106.
[15] Rizzo FJ. An integral equation approach to boundary value problems of classical elastostatics. Q Appl Math 1967;25:83–95.